Imaging-based amplitude laser beam shaping for material processing by 2D reflectivity tuning of a spatial light modulator

JIANGNING LI[1], ZHENG KUANG[1,*], STUART EDWARDSON[1], WALTER PERRIE[1], DUN LIU[2], GEOFF DEARDEN[1]

[1]*Laser Group, Centre for Materials and Structures, School of Engineering, University of Liverpool, Brownlow Street, Liverpool L69 3GQ, UK*
[2]*School of Mechanical Engineering, Hubei University of Technology, Wuhan 430068, China*
**Corresponding author: z.kuang@liv.ac.uk or kz518@msn.com*

We have demonstrated an original ultrafast beam shaping and intensity modifying technique for material processing using a spatial light modulator (SLM). Intensity masks with 256 gray levels were designed to shape the input laser beam in both outline profile and inside intensity distribution. Squared and circular flat-top beam shapes were obtained at the diffractive near-field and then reconstructed at an image plane of an f-theta lens (f ~ 100mm). The observed intensity distribution inside the beam shaping geometry was much more even than using binary masks. The ablation footprint well matches the desired beam shape.

1. INTRODUCTION

In recent years, ultrashort pulse lasers, i.e. femtosecond (fs) or picosecond(ps) lasers, have attracted increasing interests as a high precision and quality tool for micro-processing on various materials. Metals [1] [2], semiconductors [3], dielectrics [4] [5] [6] and biological materials [7] [8] have been processed by ultrashort pulse laser to generate a very small heat affected zone around the irradiated area. Compared to fs lasers, ps lasers are more compact, lower cost and may have more efficient and accurate material processing ability [9] [10]. Hence, ps laser systems, such as fibre lasers, have been widely employed by manufacturing industries.

One of the characteristics of ultrashort pulse laser material processing is that the shape of the processed area is very close to the input beam's intensity distribution thanks to the well-defined ablation threshold. This has motivated some efforts in the field of ultrashort pulse laser beam shaping. From the use of amplitude mask projection and diffractive optical elements (DOEs) [11] to deformable mirrors [12], different techniques have been attempted to shape ultrashort pulse laser beams for various applications. Multiple annular beams were generated at focal plane for ultrashort pulse laser micro-drilling with diffractive axicon phases using a spatial light modulator (SLM) [13]. Sanner et al. successfully obtained top-hat, doughnut, square, and triangle beam shapes at focal plane by programmable wave-front modulations using a non-pixelated optically addressed light valve [14] [15].

The phase modulation to the incident laser beam can be complicated in order to produce a desired shape at focal plane (i.e. far field). Although algorithms based on time-consuming iterative calculations, such as Gerchberg and Saxton [16] [17] [18], were attempted to calculate the phase holograms for the far field beam shaping, the accuracy was still not perfect due to the complex nature of light diffraction. In order to produce good beam profiles in terms of accuracy, flexibility, and speed, imaging-based phase modulation has also been demonstrated to produce high-precision amplitude and phase modulation [19] [20] [21]. Besides phase modulation, imaging-based amplitude beam shaping techniques have been used to produce high-precision beam profiles with arbitrary shapes [22] [23] [24].

We recently demonstrated an interesting imaging-based amplitude beam shaping technique using a spatial light modulator (SLM), where arbitrary beam intensity shapes were easily obtained by binary (i.e. black and white) geometric masks at diffraction near-field and then reconstructed at an imaging plane with a much smaller size comparable to the beam waist at focal plane [25]. Due to the high-energy damage threshold of the SLM, this technique is exceptionally well suited for high power laser material processing. However, the binary geometric masks only shaped the outline of the beam profile but left the area inside the geometry unchanged, hence significantly limited the shaping ability. Some beam shapes (e.g. flat-top) commonly used in industry cannot be achieved only using binary geometric masks.

In this paper, intensity grey level (0-255) geometric masks were used to fully shape the input laser beam (outline and inside area of the shaping geometry). Squared and circular flat-top beam shapes were created at the diffractive near-field and then reconstructed at an image plane of an f-theta lens (f ~ 100mm). The observed intensity distribution inside the beam shaping geometry was much more even than using binary masks. The flat-top beam machined footprints demonstrated significant improvement in the bottom uniformity. This could lead to industrial applications, such as high accuracy thin-film processing, high uniformity laser induced periodic surface structuring (LIPSS) and high efficiency surface treatment.

2. EXPERIMENTAL AND METHODOLOGY

A. Experimental setup

A schematic of the experimental setup is shown in Fig.1. A linear polarized laser beam output (Beam diameter: Dia. ≈ 0.8mm, pulse duration: tp= 20ps, wavelength: λ = 1064nm, and repetition rate: F=200 kHz) from a picosecond fibre laser system (Fianium) passed through a half wave plate used for adjusting the polarisation direction, a beam expander (M ≈ ×6), two plane mirrors for controlling the beam path, and illuminated on a reflective, liquid crystal SLM (Holoeye LC-R 2500). A polarization analyzer was placed after the SLM to modulate the intensity of laser beam. When observing the beam profile, the laser beam was reflected by a flip mirror and then passed through two positive lenses (focal length: f_0 = 200mm) form a 4f system to reach a CCD camera-based laser beam profiler (Thorlabs). When processing, the flip mirror was removed from the optical alignment. The beam hence traversed a long distance by multiple reflections on a series of mirrors before reaching a scanning galvanometer, and a focusing F-theta lens ($f_{f\text{-}\theta}$ =100mm). Machining samples were mounted on a three-axis (x,y,z) motion control stage (Aerotech), placed under the F-theta lens.

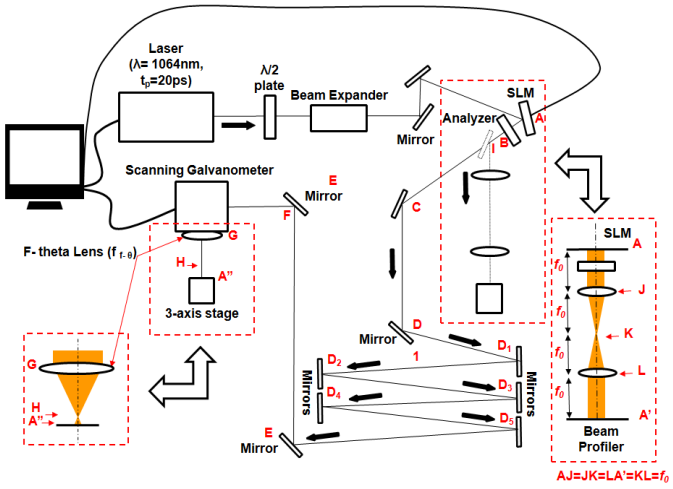

Fig. 1. Experimental setup.

B. Generation of flat-top beam using grey level gradient masks

Holoeye LC-R 2500 is a reflective Liquid Crystal on Silicon (LCoS) based spatial light modulator (SLM). The structure of the LCoS is 45 degree twisted nematic (TN) microdisplay cells. When applying an input voltage signal from 0 to maximum (controlled by mask's grey level from 0 to 255), the orientation of the molecules changes accordingly by 0 – 45 degree between the top and the bottom of the LC cell, creating a helix-like structure. The output polarization hence varies from 0 to 45 degree accordingly. By using a geometric grey level gradient mask and a polarization analyzer placed after SLM, an accurate amplitude modification can be achieved.

Fig.2 shows the reflectivity (R) versus the grey level of the mask. The relationship between R and GL is approximately linear, as shown in figure 2.

$$\mathbf{R = f(GL) = 0.001GL + 0.2006} \qquad \textbf{(1)}$$

where GL is the mask gray level, GL ϵ [0 , 255].

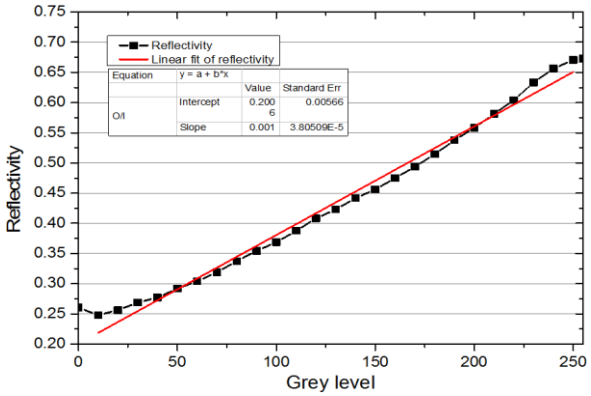

Fig. 2. The SLM reflectivity versus mask grey level.

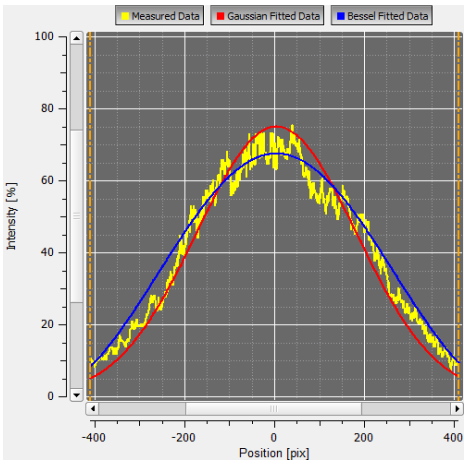

Fig. 3. Intensity distribution along beam diameter

Fig.3 shows that the original laser beam profile (y) well matched the Gaussian distribution (red line) in equation (3).

$$\mathbf{y = \frac{1}{\sigma\sqrt{2\pi}} e^{\frac{-x^2}{2\sigma^2}}} \qquad \textbf{(2)}$$

where σ is calculated to be 2.03 (unit: 100pixels), based on the data shown in figure 3. Thus, y becomes:

$$\mathbf{y = g(x) = \frac{1}{5.08} e^{\frac{-x^2}{8.24}}} \qquad \textbf{(3)}$$

Since the shaped beam profile is the product of the original beam profile (y) and the reflectivity of SLM (R), a flat top distribution can be obtained when:

$$\mathbf{y \times R = c} \qquad \textbf{(4)}$$

where c is a constant. By combining equation (3) with (4), the distribution of reflectivity (R) becomes:

$$\mathbf{R = m e^{\frac{x^2}{8.24}}} \qquad \textbf{(5)}$$

where m = 5.08c. By combining equation (1) and (5), we can derive:

$$\mathbf{m e^{\frac{x^2}{8.24}} = 0.001GL + 0.2006} \qquad \textbf{(6)}$$

Since σ ≈ 2 (unit: 100pixels), x ϵ [-2,2] (i.e. the length of 400pixels, corresponding to ≈ 2.6mm) was set to define the size of geometric mask.

Figure 4 shows how the original Gaussian profile (y) is shaped to flat-top (y') with the intensity mask that modulates the reflectivity of SLM (R).

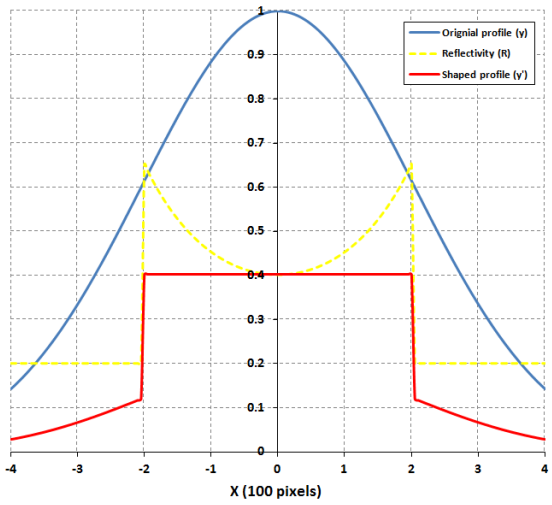

Fig. 4. Gaussian profile (y) shaped to flat-top (y') with the intensity mask that modulates the reflectivity of SLM (R) - $y' = y \times R$

when x=±2 (i.e. the edge of the mask geometry), the reflectivity (R) should reach the maximum and GL hence should be 255, based on figure 2. So, m is calculated to be 0.277. Thus:

$$\mathbf{GL} = \frac{0.277e^{\frac{x^2}{8.24}} - 0.20}{0.001} \quad \textbf{(7)}$$

where x ϵ [-2,2]. Based on equation 7, intensity masks with various shapes were created using Matlab. As shown in figure 5, two GL gradient masks were created to shape the beam to (a) circle flat top and (b) square flat top.

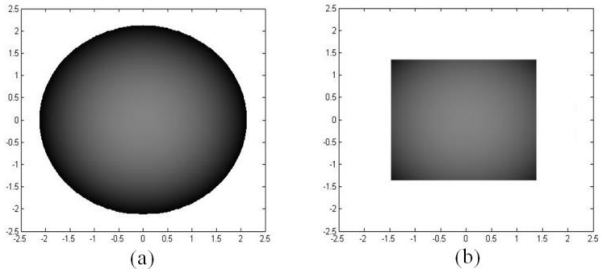

Fig. 5. Grey level gradient masks generated by Matlab.

C. Shaping reconstruction at imaging plane of focusing lens

As shown in figure 1, the generated mask shaped the incident beam in near field after SLM at A. The shape was reconstructed after the 4-f optical system at A' for the observation using the beam profiler, and also reconstructed at the imaging plane of the F-theta lens, A", for the material processing. As shown in Figure 1, five extra mirrors, D1–D5, were added to significantly increase the distance from the SLM to the focusing F-theta lens, i.e. the object distance. The purpose of this was to reconstruct the shape to a small size comparable to the beam waist. The position of the imaging plane A″ can be calculated, based on the thin lens imaging equation below,

$$\frac{1}{u} + \frac{1}{v} = \frac{1}{f} \quad \textbf{(8)}$$

where, $\boldsymbol{u \approx 11000mm}$ is the object distance, i.e. the distance from the SLM(A) to the F-theta lens(G), f = 100mm is the focal length of the F-theta lens and v is the image distance, hence the distance from the F-theta lens(G) to image plane (A") is,

$$\boldsymbol{v = \frac{fu}{u-f} \approx 100.9mm} \quad \textbf{(9)}$$

while the separation between the focal and imaging plane is:

$$\boldsymbol{d = v - f \approx 0.9mm} \quad \textbf{(10)}$$

The magnification of the image system is $\mathbf{M \approx 1/110}$. The diameter of reconstructed beam at A" can be calculated to be approximately 34.5μm, which was comparable to the beam waist at the focal plane H.

3. RESULTS AND DISCUSSIONS

A. Beam shaping results observed by CCD camera at A'

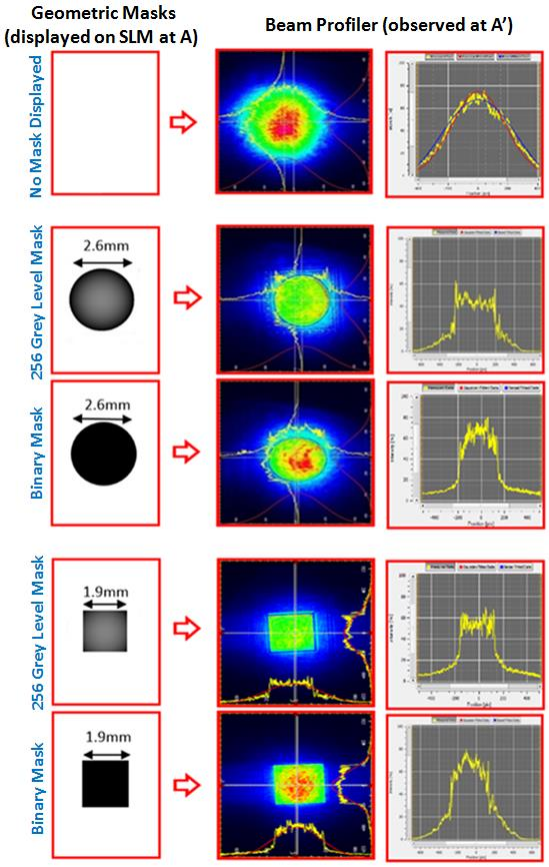

Fig. 6. Comparison between the binary and 256 grey level masks shaping results - First line: geometric masks applied on the SLM. Second line and Third line: 2D beam profile and intensity distribution across the beam diameter, observed by the beam profiler at A'

As shown in figure 6, the first line shows geometric binary and grey level masks applied to the SLM, while the second and the third line show the corresponding beam profiles observed at A' and intensity distribution along the beam diameter, respectively. The binary masks only shaped the outline profile but left the inside intensity distribution essentially unchanged, while the 256 grey level masks shaped both the

outline profile and the inside intensity distribution, hence successfully created circular and spared flat-top beams.

B. Shaped beam machining results at A"

Figure 7 and 8 shows the circular and squared flat-top beam machined results, respectively. The beam was shaped using the binary (upper) and 256 grey level masks (lower). Footprints were fabricated on a polished stainless steel sample by the shaped laser beams at the image plane A". The input laser pulse energy (Ep) was approximately 2.1 μJ, measured before the scanning galvanometer aperture. Since the laser frequency was F = 200kHz repetition rate and the drilling time for each footprint was 1s., ~200k pulses were used to fabricate each footprint. The machined footprints were then observed using the white light interferometer (WYKO). As shown in figure 6, the footprints fabricated by binary masks show an approximately Gaussian shaped bottom indicating that the inside beam intensity distribution was unshaped, while the footprints fabricated by 256 grey level masks demonstrated a relatively flat bottom. This demonstrates a good match between the footprint shapes machined at the image plane at A" and the created beam shapes observed at A', as shown in figure 6.

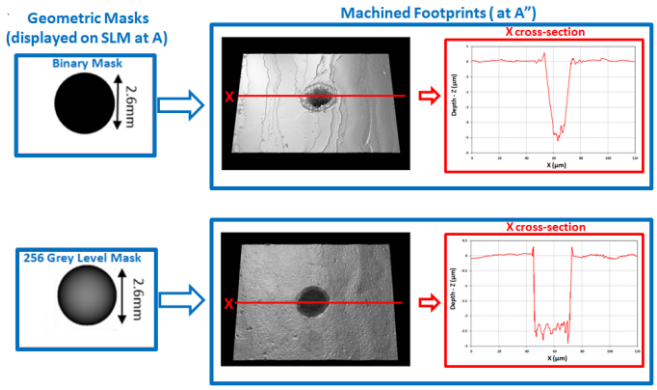

Fig. 7. Comparison between binary and 256 grey level masks machining results (circular flat-top) – upper: using binary mask; lower: using 256 grey level mask

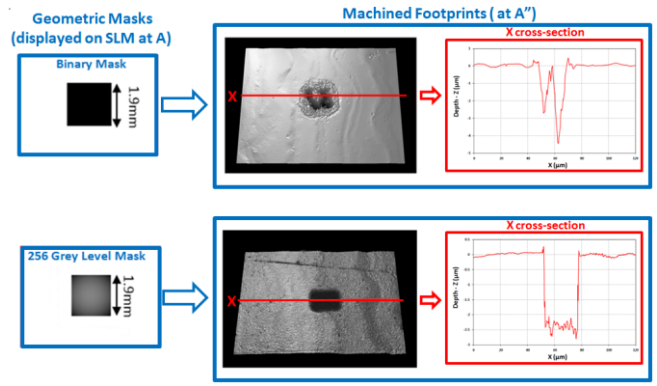

Fig. 8. Comparison between binary and 256 grey level masks machining results (squared flat-top) – upper: using binary mask; lower: using 256 grey level mask.

C. Shaping quality and efficiency vs. the size of mask

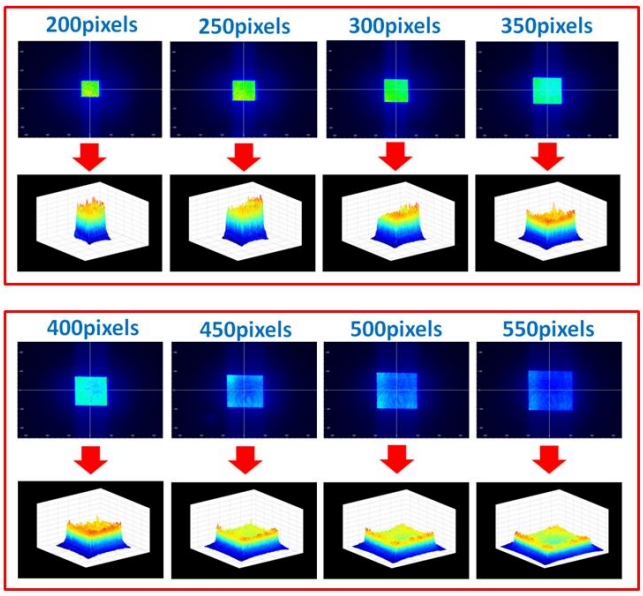

Fig. 9. Shaping by varying mask size (side length of mask varied from 200 to 550pixels)

Both shaping quality and efficiency may change when varying the size of geometric mask. Figure 9 shows the shaped beam profile observed at A' when varying the mask size (side length varied from 200 to 550pixels).

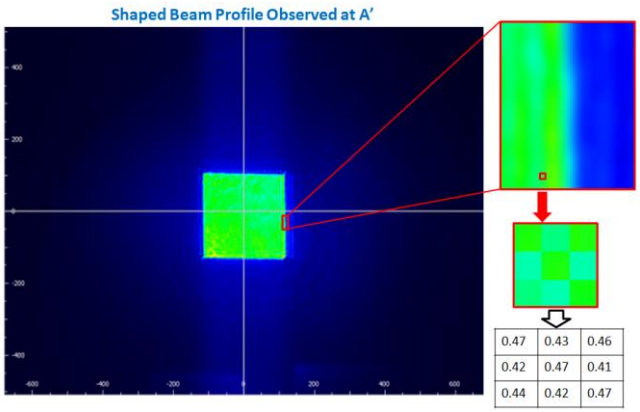

Fig. 10. Analysis of shaped beam profile observed at A'

In order to quantitatively study the beam quality variation, images of shaped beam profile observed at A' were analyzed by Matlab. As shown in figure 10, the lower right corner matrix was extracted, which quantitatively demonstrated the intensity distribution in a tiny area (3×3 pixels). Accordingly, an entire shaped area matrix can be extracted. The roughness rate (R) of shaped area can be calculated using the equation below:

$$\mathbf{R} = \frac{\sigma}{\mathbf{M}} \times \mathbf{100\%} \qquad \textbf{(11)}$$

where M is the mean value of all the number in the shaped area matrix and σ is the standard deviation. Thus, when shaping the beam to flat-top, the shaping quality can be quantitatively presented by R.

Figure 10 shows the roughness rate against the size of the geometric mask used for square flat-top shaping. When the side length of mask were between 200 and 550 (unit:100pixels), the roughness rates were measured below 10%, indicating good shaping quality.

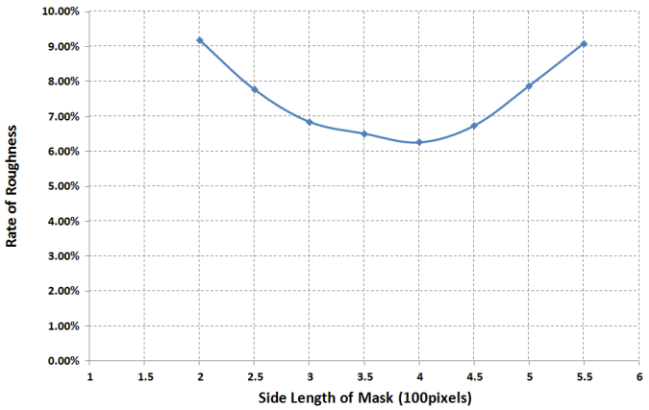

Fig. 10. Shaping efficiency (rate of roughness) against the size of the mask

Shaping efficiency can be calculated using the equation below.

$$\eta = \frac{\oint \mathbf{I_{shaped}} \mathbf{dS}}{\oint \mathbf{I_0} \mathbf{dS}} \times 100\% \qquad (12)$$

where $\oint \mathbf{I_{shaped}}\ \mathbf{dS}$ is the integral of the shaped beam intensity profile and $\oint \mathbf{I_0}\ \mathbf{dS}$ is the integral of the original beam intensity profile obtained at A'.

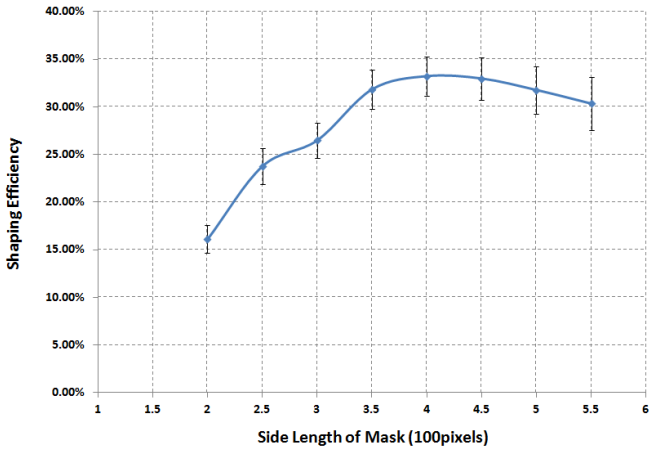

Fig. 11. Shaping efficiency against the the size of the mask

Figure 11 demonstrates shaping efficiency against the size of the mask. As shown, when the mask side length was set around 4 (unit: 100pixels), the shaping efficiency reached the highest. This is probably because the highest shaping efficiency can be achieved when the rectangular area (A) under the Gaussian curve reaches the maximum (A_{max}), as shown in figure 12. According to equation (3),

$$\mathbf{A = f(x) = 2xy = 2xg(x) = \frac{2x}{5.08} e^{\frac{-x^2}{8.24}}} \qquad (13)$$

Thus, A_{max} is reached when:

$$\frac{\mathbf{df(x)}}{\mathbf{dx}} = \mathbf{0} \qquad (14)$$

By solving the formula (14), we get that the highest shaping efficiency is achieved when x ≈ 2, i.e. the side length of mask = 2x ≈ 4 (unit: 100pixel).

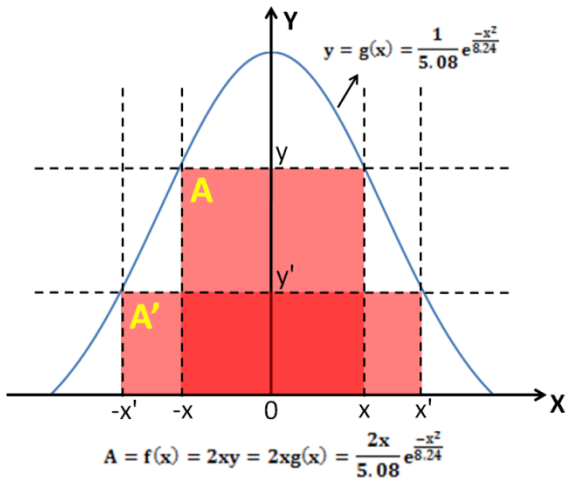

Fig. 12. How to maximize the shaping efficiency

3. CONCLUSIONS

A novel ultrashort pulse laser beam shaping technique to generate geometric flat top beams were demonstrated in this paper. Grey level geometric masks designed according to the original beam profile were applied on a spatial light modulator (SLM) to control the shape and intensity distribution of the reflected laser beam. A near Gaussian intensity beam was thus effectively converted to round or square flat-top with uniform intensity which were then reconstructed at the imaging plane of a focusing lens. A polished titanium sample was machined by the shaped beam at the imaging plane. The machined footprint has the corresponding shape and depth distribution of the beam. Although there were low intensity wings, the fluence in these was well below ablation threshold so that sharp walls resulted. This novel beam shaping technique has potential applications, such as uniform LIPSS production, and thin film processing using such geometric and intensity distribution shaped laser beams.

ACKNOWLEGEMENTS

The co-author Dun Liu would like to acknowledge the support form National Natural Science Foundation of China (No. 11204071)

References

1. C. Momma, B. Chichkov, S. Nolte, F. von Alvensleben, A. Tunnermann and H. Welling, "Short pulse laser ablation of solid targets," Opt Commun, no. 129, pp. 134-42, (1996).
2. D. Vonder Linde and K. Sokolowski-Tinten, "The physical mechanisms of short-pulse laser ablation," Appl Surf Sci, no. 154-155, pp. 1-10, 2000.
3. S. Sundaram and E. Mazur, "Inducing and probing non-thermal transitions in semiconductors using femtosecond laser pulses," Nat mater, no. 1, pp. 217-24, (2002).
4. L. Sudrie, M. Franco, B. Prade and A. Mysyrowic, "Study of damage in fused silica induced by ultra-short IR laser pulses," Opt Commun, no. 191, pp. 333-9, (2001).
5. C. Schaffer, A. Jamison and E. Mazur, "Morphology of femtosecond laser-induced structral changes in bulk transparent materials," Appl phys lett, no. 84, pp. 1441-3, (2004).
6. R. Osellame, S. Taccheo, M. Marangoni, R. Ramponi, P. Laporta and D. Polli, "Femtosecond writing of active optical waveguides with astigmatically shaped beams," J Opt Soc Am B, no. 20, pp. 1559-67, (2003).
7. K. Konig, O. Krauss and I. Riemann, "Intratissue surgery with 80-MHz

nanojoule femtosecond laser pulses in the near infrared," Opt Express, no. 20, pp. 171-6, (2002).

8. W. Watanabe, N. Arakawa, S. Matsunaga, T. Higashi, K. Fukui and K. Isobe, "Femtosecond laser disruption of subcellular organelles in a living cell," Opt Express, no. 12, pp. 4203-13, (2004).
9. F. Dausinger, Machining of metals with ultrashort laser pulses: from fundamental investigations to industrial applications, Proc. SPIE 5777 840. (2005).
10. J. Cheng, W. Perrie, M. Sharpe, S.P. Edwardson, N.G. Semaltianos, G. Dearden, K.G.Watkins, Single-pulse drilling study on Au, Al and Ti alloy by using a picoseconds laser, Appl. Phys. A 95 739–746, (2009).
11. C. Momma, S. Nolte, G. Kamlage, F. von Alvensleben and A. Tunnemann, "Beam dilivery of femtosecond laser radiation by diffractive optical elements," Appl PhysA, vol. 67, pp. 517-20, (1998).
12. R. R. Thomson, A. S. Bockelt , E. Ramsay, S. Beecher, A. H. Greenaway and A. K. Kar, "Shaping ultrafast laser in scribed optical wave guides using a deformable mirror," Opt Express, vol. 16(17), pp. 517-20, (2008).
13. Z. Kuang, W. Perrie, S. Edwardson, E. Fearon and G. Dearden, "Ultrafast laser parallel micro drilling using multiple annular beams generated by a spatial light modulator," JPhysD:Applphys, vol. 47, p. 115501, (2014).
14. N. Sanner, N. Huot, E. Audouard and C. Larat, "Programmable focal spot shaping of amplified femtosecond laser pulses," Opt Lett, vol. 30(12), pp. 1479-81, (2005).
15. Sanner N, N. Huot, E. Audouard, C. Larat and J. Huignard, "Direct ultrafast laser micro-structuring of materials using programmable beam shaping" Opt Laser Eng, vol. 45, pp. 737-41, (2007).
16. R. Gerchberg and W. O. Saxton , "A practical algorithm for the determination of the phase from image and diffraction plane pictures," Optik, vol. 35, p. 237, (1972).
17. J. S. Liu and M. R. Taghizadeh, "Iterative algorithm for the design of diffractive phase elements for laser beam shaping," Opt Lett, vol. 27, p. 1463, (2002).
18. R. Beck, J. Parry, J. Shephard and D. Hand, "Adaptive extra cavity beam shaping for application in nanosecond laser micromachining," *Proc. SPIE* 7913, Laser Resonators and Beam Control XIII, 79130D (February 18, 2011); doi:10.1117/12.875177.
19. Independent phase and amplitude control of a laser beam by use of a single-phase-only spatial light modulator", Optics Letters 29(3), 295-297 (2004).
20. Fast conversion of digital Fresnel hologram to phase-only hologram based on localized error diffusion and redistribution", Optics Express 22(5), 5060-5066 (2014).
21. GPC light shaping a supercontinuum source", Optics Express 23(3), 1894-1905 (2015).
22. Dynamic spatial pulse shaping via a digital micromirror device for patterned laser-induced forward transfer of solid polymer films", Optical Materials Express 5 (5), 1129-1136 (2015).
23. High-brightness X-ray free-electron laser with an optical undulator by pulse shaping", Optics Express 21 (26), 32013-32018 (2013).
24. A high-resolution, adaptive beam-shaping system for high-power lasers," Optics Express 18 (9), 9151–9162 (2010).
25. Z. Kuang, J. Li, W. Edwardson, W. Perrie, D. Liu and G. Dearden, "Ultrafast laser beam shaping for material processing at imaging plane by geometric masks using a spatial light modulator," Optics and Laser in Engineering, vol. 70, pp. 1-5, (2015).